

Multiscale modelling of hydrogen behaviour on beryllium (0001) surface



Ch. Stihl*, P.V. Vladimirov

Institute for Applied Materials – Applied Materials Physics, Karlsruhe Institute of Technology, 76344, Eggenstein-Leopoldshafen, Germany

ARTICLE INFO

Article history:
Available online 29 August 2016

Keywords:
Ab initio
First principles
Beryllium
Hydrogen
Deuterium
Tritium
Interaction
Surface
Reconstruction
Multiscale modeling
Dimer method

ABSTRACT

Beryllium is proposed to be a neutron multiplier and plasma facing material in future fusion devices. Therefore, it is crucial to acquire an understanding of the microscopic mechanisms of tritium accumulation and release as a result of transmutation processes that Be undergoes under neutron irradiation. A multiscale simulation of ad- and desorption of hydrogen isotopes on the beryllium (0001) surface is developed. It consists of ab initio calculations of certain H adsorption configurations, a suitable cluster expansion approximating the energies of arbitrary configurations, and a kinetic Monte Carlo method for dynamic simulations of adsorption and desorption. The processes implemented in the kinetic Monte Carlo simulation are deduced from further ab initio calculations comprising both, static relaxation as well as molecular dynamics runs. The simulation is used to reproduce experimental data and the results are compared and discussed. Based on the observed results, proposals for a refined model are made.

© 2016 Published by Elsevier Ltd.

This is an open access article under the CC BY-NC-ND license (<http://creativecommons.org/licenses/by-nc-nd/4.0/>).

1. Introduction

Future fusion devices like ITER and DEMO are proposed to deploy beryllium as a plasma facing material for the first wall [1] and neutron multiplier in tritium breeding blankets [1–3]. Within the helium cooled pebble bed blanket (HCPB), lithium ceramics are used as the actual tritium breeding material while beryllium acts as a neutron multiplier, thus providing for a self-sustained tritium fuel cycle. As the fusion plasma emits highly energetic neutrons, beryllium undergoes transmutation reactions generating considerable amounts of helium and tritium [4] as a result. With the accumulation of these reaction products, gas filled bubbles emerge [5] as tritium and helium are captured by vacancies which coalesce. These processes also lead to considerable degradation of material properties [6]. The inner surfaces of gas filled bubbles as well as the outer surfaces of plasma facing Be tiles imply a pronounced importance of the interactions of hydrogen isotopes with beryllium surfaces, which will ultimately need to include interactions of (pre)adsorbed hydrogen. Regarding safety concerns, assessment of the radioactive tritium inventory trapped inside beryllium pebbles and the handling of radioactive beryllium waste after the end-of-life of the blanket are very important for the actual oper-

ation of a fusion reactor. Therefore, it is crucial to acquire a thorough understanding of the microscopic mechanisms of tritium retention and release, naturally including a faithful representation of mechanisms at surfaces.

Therefore, numerous experimental and theoretical studies have been conducted to gain insight into the governing mechanisms of tritium retention and release.

Typical experiments consist of exposing beryllium samples to hydrogen isotope gases [7–9], hydrogen isotope ion implantation beams [10–15], or neutron irradiation [5,6], all of which resulting in the accumulation of hydrogen isotopes within the beryllium samples. Subsequently, an array of experimental techniques like low-energy ion scattering (LEIS) [13], X-ray photoelectron spectroscopy (XPS) [13], low-energy electron diffraction (LEED) [9], high-resolution electron-energy-loss spectroscopy (HREELS) [9], nuclear reaction analysis (NRA) [9], transmission electron microscopy (TEM) investigations [10], and/or temperature programmed desorption (TPD) spectroscopy [7,8,12–14] are routinely applied to either directly track the hydrogen isotope behaviour within the samples or deduce it from the data taken. Especially TPD spectra, which aim to establish a mapping from desorption rate peak temperatures to activation energies and therefore atomic scale desorption processes, leave a wide field of possible, competing explanations for several similar features.

Typical theoretical studies are usually based on ab initio, i.e. density function theory (DFT) calculations. There are numerous

* Corresponding author.

E-mail addresses: christopher.stihl@kit.edu (Ch. Stihl), pavel.vladimirov@kit.edu (P.V. Vladimirov).

publications relevant to beryllium surfaces and their interactions with hydrogen, see e.g. [16,17] and [18–21], respectively. For the (0001) beryllium surface, there is a rather well established consensus of hydrogen atomically adsorbing at two stable sites for low hydrogen concentrations on the surface. These sites are named the fcc and hcp adsorption sites, with the latter one being energetically more favourable. Here, we adopt the notion of a coverage relative to those adsorption sites, i.e. a coverage of 1.0 corresponds to all fcc and hcp adsorption sites being occupied. Significantly more uncertainty is attributed to regimes of higher coverages. The two-fold coordinated bridge sites right between the fcc and hcp adsorption sites becoming stable adsorption sites at a coverage of 0.5 is a rather well established finding our calculations agree with. Some publications suggest these bridge sites are available in addition to hcp and fcc sites, e.g. [22]. At those coverages, the energetical hierarchy of fcc and hcp adsorption sites is reversed and the bridge site is now the new groundstate adsorption site. However, our calculations also indicate the bridge site replaces the fcc and hcp adsorption sites instead of becoming available for adsorption in addition.

Based on ab initio calculations performed by us, a multiscale modelling approach to hydrogen ad- and desorption deploying our own atomic kinetic Monte Carlo (kMC) code was developed. The goal of this work is to establish the overall validity of our approach by reproducing aspects of actual experiments. To this end, we focus on modelling of atomic deuterium exposure experiments undertaken by Lossev and Kueppers [7,8].

2. Simulation methods

Our multiscale modelling approach is based on ab initio calculations carried out using the Vienna Ab initio Simulation Package (VASP) [23,24] in terms of static energy minimization and microcanonical first principles molecular dynamics runs. The projector augmented wave (PAW) potentials as shipped with VASP [25,26] are used for beryllium and hydrogen, modelling beryllium with two valence electrons. For molecular dynamics runs, the atomic mass in the H potential was changed to that of deuterium mass (2.014) via the POMASS-tag in the POTCAR file. The exchange-correlation energy is approximated by the generalized gradient approximation (GGA) according to Perdew and Wang [27]. Moreover, a Fermi broadening as proposed by Methfessel and Paxton [28], a smearing width of 0.2 eV, and a cutoff energy of ENCUT = 450 eV were deployed. The bulk lattice constants $a = b = 2.263$ Å and $c = 3.569$ Å were calculated using these parameters. Throughout all calculations, the k-point grid sampling is done on a gamma centred grid not less dense than $31 \times 31 \times 1$ for a surface simulation cell with lateral lengths of only one unit cell as this has been explicitly confirmed to yield well converged total energies. Total energy convergence with significantly more dense k-point grids was occasionally ensured for laterally larger simulation cells with different lateral geometries, though. All surface simulation cells include a vacuum gap of more than 18.5 Å after full relaxation in order to get rid of unintentional interactions due to periodic boundary conditions.

Utilizing ab initio calculation results in subsequent stages of the multiscale simulation chain requires a high quality parametrization of total energies. For discrete systems, a state of the art parametrization is given by the cluster expansion (CE) formalism [29]. This expansion systematically expands total energies E for arbitrary parent lattice occupations $\vec{\sigma} = (\sigma_1, \dots, \sigma_N)$ denoted by spin variables σ_i on N sites according to

$$E(\vec{\sigma}) = \sum_{\alpha \in A} m_{\alpha} J_{\alpha} \langle \prod_{i \in \alpha'} \sigma_i \rangle, \quad (1)$$

with summation over clusters α symmetrically inequivalent and averaging over clusters α' symmetrically equivalent to α under

parent lattice spacegroup operations. To that end, effective cluster interaction (ECI) energies J_{α} need to be found for a considered set of clusters A , associating each cluster α to an energy contribution via multiplicities m_{α} and the occupation dependent correlation $\langle \prod_{i \in \alpha'} \sigma_i \rangle_{\alpha'}$.

The adsorption layer can be taken as a substitutional alloy composed of hydrogen (H) and vacancies Vac. In this alloy, the two species reside in the fcc and hcp sites which compose the two dimensional parent lattices. That way, the problem is mapped to finding a cluster expansion for a substitutional alloy and the MIT Ab initio Phase Stability (MAPS) code can be used. MAPS searches for a cluster expansion truncation in an iterative manner. At each iteration, MAPS starts by choosing an optimal truncation as indicated by a minimal leave-one-out cross validation (CV) score. The set of trial truncations at this step is limited by a physically plausible heuristic based on the complexity (number of sites) and size (largest pair distance) of the clusters. Subsequently, MAPS proposes a new configuration to include in the training set on the grounds of the best truncation so far. This new configuration either corresponds to a newly predicted ground state or results in the most reduction of the variance component in the least square fit prediction error. If a truncation fails to reproduce the ground state hull, the relative weight of the offending configurations is increased and an iterative refitting scheme is applied.

For the purpose considered in this work, the actual input energies for MAPS are given by

$$E(\vec{\sigma}) = E_{\text{ads},\sigma} = E_{\text{total}} - n_{\text{uc}} E_{\text{uc}} - n_{\text{H}} \frac{E_{\text{H}_2}}{2}, \quad (2)$$

with the total energy of the considered configuration as provided by VASP E_{total} , the size of the simulation cell in multiples of surface unit cell n_{uc} , the total energy of the clean surface unit cell E_{uc} , the number of adsorbed H atoms n_{H} , and the total energy of the H_2 molecule $E_{\text{H}_2} = -6.719$ eV. Small changes within the MAPS code enable an automated adoption of all cluster expansions obtained by MAPS in our own kMC code which is described at the end of this chapter.

To obtain estimates of typical barriers for dissociative adsorption processes, microcanonical molecular dynamics runs were carried out. The setup of those runs generally consist of a D_2 projectile and a fully relaxed Be slab at 0 K. The initial velocities of the ions in the molecule result in a suitable center of mass velocity towards a targeted impact point on the slab. The slab itself may be clean or preadsorbed with atomic H in given amounts and configurations. The actual energy barriers ΔV are then derived from utilizing the losses of kinetic energy ΔT in microcanonical ab initio molecular dynamic simulations, in which

$$E_0 = T_0 + V_0 \stackrel{!}{=} T(t) + V(t) = E(t) \quad (3)$$

$$\Rightarrow \Delta V = V(t) - V_0 = T_0 - T(t) = \Delta T \quad (4)$$

holds. Here, E_0 , T_0 , and V_0 denote the initial total, kinetic, and potential energies while $E(t)$, $T(t)$, and $V(t)$ denote the total, kinetic, and potential energies at time t . As a measure of the validity of calculations like that, the drift in total free energy $E_0 - E(t)$ was monitored. Atomic deuterium adsorption was studied using the same technique.

Estimations of the deuterium surface diffusion activation barriers ΔE for jumps between adjacent adsorption sites are calculated by

$$\Delta E = E_{\text{trans}} - E_{\text{init}} \quad (5)$$

with the energy E_{init} from a relaxed initial state, i.e. H adsorbed in a fcc or hcp site, and E_{trans} from a converged dimer calculation carried out by the method as implemented in the VASP transition state theory (VTST) [30] tools patch for VASP. To that

end, the conjugate gradient optimizer (IOPT = 2), a dimer separation of $DdR = 10^{-2}$ Å, a maximum number of consecutive rotation steps $DRotMax = 6$, and an electronic loop termination delta of $EDIFF = 10^{-7}$ eV were used. To preserve microscopic reversibility, the barriers of a diffusion process and its reverse process need to be estimated in a consistent manner. This is achieved by calculating the actual barrier ΔE_{bar} according to

$$\Delta E_{\text{bar}} = \Delta E + \max\{E_{\text{pre}}, E_{\text{post}}\} - E_{\text{pre}}. \quad (6)$$

with the system energy before the proposed diffusion step E_{pre} , the system energy after the proposed diffusion step E_{post} , and ΔE given by (5). The barriers were calculated for the clean beryllium surface and for a maximum of additional H adsorbed in the immediate vicinity n_{max} . The effect of additional H in the immediate vicinity n_{add} of the hopping H is then accounted for by a simple linear interpolation scheme

$$\Delta E = \frac{n_{\text{add}}}{n_{\text{max}}} \Delta E(n_{\text{max}}) + \frac{n_{\text{max}} - n_{\text{add}}}{n_{\text{max}}} \Delta E(0). \quad (7)$$

That is, if there were for instance $n_{\text{add}} = 3$ additional H in second nearest neighbor sites and $n_{\text{max}} = 4$, the considered diffusion hop barrier would be estimated according to $\Delta E = \frac{3}{4} \Delta E(4) + \frac{4-3}{4} \Delta E(0)$. The actual upper and lower bounds are reported as a part of the corresponding results in Section 3.2.2.

The energy barriers of associative desorption processes on the clean surface are calculated using the dimer method with algorithmic parameters just as described above. The dependence of the barrier height on additional H adsorption in neighbouring sites is slightly more complex, details are presented below in Section 3.2.3.

The implemented kMC code is based on the rigid parent lattice notion as described above in the cluster expansion context. The code mainly is a rather straight-forward implementation of the “one process at a time”-approach, the kMC method is based on. [31] Parsing in output generated by small modifications within the MAPS code, the kMC code automatically determines which cluster correlations need to be updated due to an occupation change in a given site.

Within the conventional process management, the kMC code chooses one process at random with a probability proportional to its respective rate at each iteration. For the time accounting, the simulation time is then advanced by a random increment inversely proportional to the total sum of the rates of all processes. This approach is well known as the residence time kMC algorithm. Our code differs from that in considering “instantaneous” processes. These processes are chosen from a separate process list before the conventional process management is invoked and the simulation time is not advanced. This is done exhaustively in the sense that the code continues with the conventional process management only after this “instantaneous” process list has been exhausted. These processes can thus be thought of as having no barriers associated with them. Their particular physical meaning and the corresponding motivation of their introduction will become clear in the discussion in Section 4.

Fig. 1 summarizes how the different codes are combined in our overall multiscale simulation approach.

3. Results

3.1. Cluster expansion truncation

The cluster expansion (CE) truncation is based on a training set of 57 configurations. It reproduces the ground state hull of the ab initio calculations within the required concentration interval [0.0, 0.49] and uses 21 clusters. Among them are two-site clusters with diameters (of up to ≈ 5.695 Å) corresponding to ninth nearest neighbours and three-site clusters with diameters of (up to

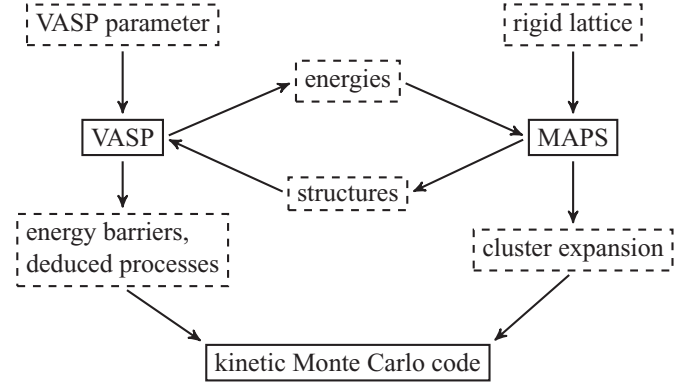


Fig. 1. Sketch of the codes comprising our multiscale simulation approach and their interplay. Solid boxes indicate codes, dashed boxes information, and arrows indicate in- and output of codes.

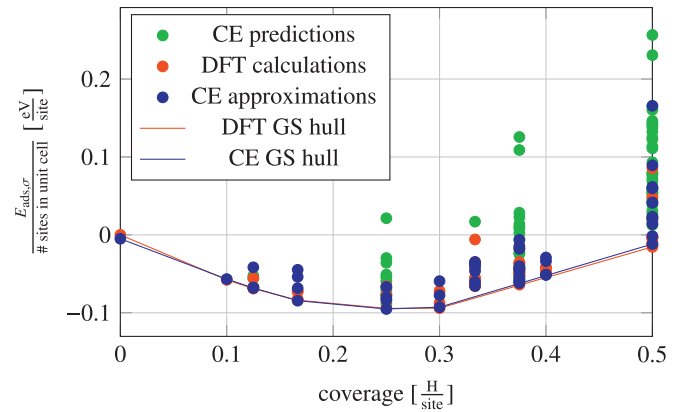


Fig. 2. Adsorption energy $E_{\text{ads},\sigma}$, see (2), per site as a function of surface coverage as found by the MAPS cluster expansion (CE) and DFT.

≈ 2.613 Å) corresponding to third nearest neighbours. The truncation thus consists of the set of 21 ECI (the free parameters) which minimizes the CV score of a set of 57 linear equations, each representing an adsorption configuration whose energy has been calculated by VASP. No further GS configurations containing eight or less adsorption sites are predicted. An overall impression of the truncation is given by the plot in Fig. 2. In this plot, “CE predictions” denotes occupation energies only predicted by the truncation, i.e. not calculated by VASP, and “DFT calculations” denotes occupation energies calculated by VASP. The latter set of points is mirrored by corresponding data points in “CE approximations” representing the energies of the same configurations approximated using the cluster expansion truncation.

3.2. Processes

3.2.1. Dissociative adsorption

Energy barriers for dissociative adsorption are rather high (≈ 0.85 eV) according to our calculations with D_2 impacting on the clean Be surface with a kinetic energy of ≈ 1.0 eV. This holds for all simulated combinations of the D_2 center of mass impact position and orientations parallel to the surface, while additional preadsorbed H increases the barrier even further. D_2 orientations orthogonal to the surface did not adsorb at all, hinting at an even higher adsorption barrier in those cases. Fig. 3 shows a representative selection of typical adsorption barriers.

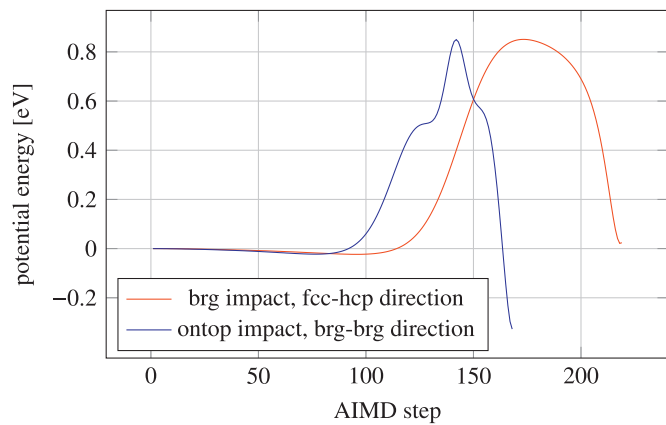


Fig. 3. Plot of two typical energy barriers of dissociative adsorption processes onto a clean surface as a function of *ab initio* MD steps. In the legend, “brg” stands for bridge, indicating the general orientation of the D_2 bond relative to the surface geometry.

Table 1

Summary of explicitly considered diffusion transition states. The barrier heights ΔE are calculated according to Eq. (5) and figures in parentheses depict the respective configurations.

Description	Lowest ΔE /eV	Highest ΔE /eV
fcc \rightarrow hcp (Fig. 4)	0.03 (Fig. 4c)	0.18 (Fig. 4b)
hcp \rightarrow fcc (Fig. 4)	0.07 (Fig. 4a)	0.21 (Fig. 4b)

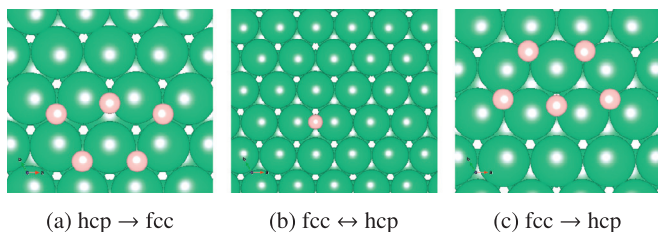


Fig. 4. Top view of surface diffusion transition state configurations. [32] Shown are the minimal ΔE configuration for hcp \rightarrow fcc in 4a, the configuration in both directions in the free case in 4b, and the lowest ΔE configuration for fcc \rightarrow hcp in 4c. Images rendered by VESTA [32].

Table 2

Summary of the explicitly considered associative desorption transition states. The barrier heights ΔE are calculated according to Eq. (5) and figures in parentheses depict the respective configurations.

Description	Lowest ΔE /eV	Highest ΔE /eV
2nn-fcc (Fig. 5)	0.99 (Fig. 5b)	1.34 (Fig. 5a)
2nn-hcp (Fig. 5)	0.97 (Fig. 5d)	1.50 (Fig. 5c)
reconst (Fig. 5)	0.97 (Fig. 5e)	0.97 (Fig. 5e)

3.2.2. Surface diffusion

Diffusion barriers are defined by (6). Dimer calculations as described in Section 2 lead to ΔE contributions summarized in Table 1. The corresponding transition states are depicted in Fig. 4.

3.2.3. Associative desorption

Associative desorption energy barriers were obtained by dimer calculations and (5), Table 2 summarizes the results and Fig. 5 depicts the corresponding transition states. Similar to surface diffusion, a simple linear interpolation with increasing H coverage between the most extreme ΔE configurations is adopted. However, it was found that, in both cases, the maximum neighbourhood coverage of 8 neighbouring H was not stable in the sense

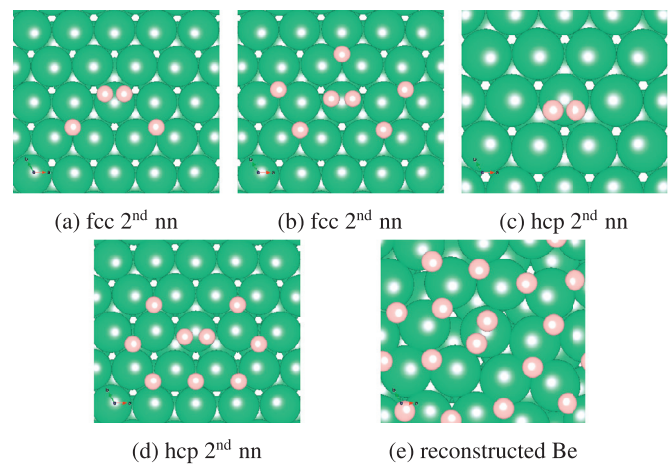


Fig. 5. Top view of explicitly considered associative desorption transition state configurations. There is the highest ΔE fcc 2nd nearest neighbor (nn) configuration in 5a, the lowest ΔE fcc 2nd nn configuration in 5b, the highest ΔE hcp 2nd nn configuration in 5c, the lowest ΔE hcp 2nd nn configuration in 5d, and the transition configuration from a Be slab with laterally reconstructed first layer Be in 5e. Images rendered by VESTA [32].

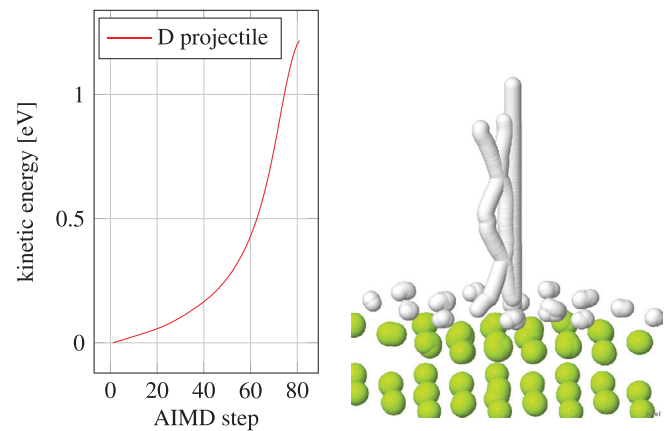


Fig. 6. (a) Acceleration of impinging D while descending towards the surface on the trajectory shown in Fig. 6b. (b) Trajectory of a MD run showing an effective desorption event. Image rendered by Jmol [33].

Fig. 6. Sketches to illustrate interactions of H with a precovered surface of 0.5 coverage as found by molecular dynamics [33].

of H hopping away from its original adsorption sites. This is considered in the actual process implementation by switching to the “reconst”-process (cf. Fig. 5e) when detecting neighbourhood coverages larger than the maximum stable ones observed.

3.2.4. Atomic adsorption

Atomic adsorption was investigated using micro canonical molecular dynamics runs as laid out in Section 2. It was found that there is no barrier for atomic adsorption. On the contrary, a pronounced acceleration of impinging H was observed. Fig. 6a shows the accumulation of ≈ 1.0 eV of kinetic energy by the impinging H due to the attraction of a preadsorbed slab with a H coverage of 0.5. In this case, an impinging H captures one of the preadsorbed H atoms and both leave the surface as a molecule, cf. Fig. 6b. The same molecular desorption was found for lower coverages when the impinging H hit an occupied adsorption site. As a result, that heuristic is adopted in the corresponding kMC process implementation, i.e. an effective desorption takes place whenever H would be put either on an occupied site or an empty adsorption

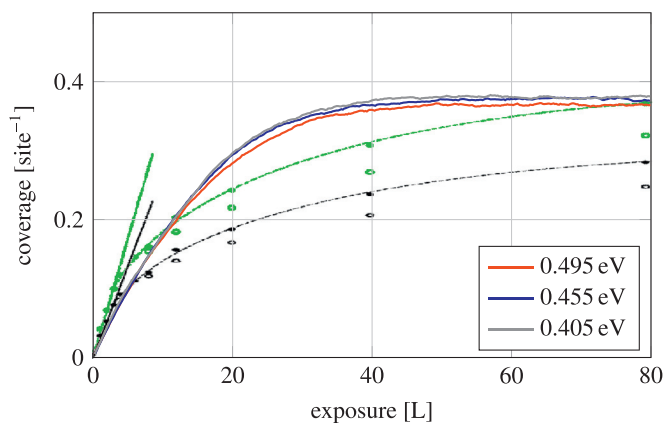


Fig. 7. Plots of data taken from several simulation runs for systems consisting of 20000 sites with significant variation of additional surface diffusion barrier offsets to control the slow down of the surface diffusion processes. The background of this overlay is given by the experimental data as found by Lossev and Kueppers [8] (black graph) and their upper error estimation boundary of 30% (green graph). (For interpretation of the references to colour in this figure legend, the reader is referred to the web version of this article.)

site with all neighbouring sites occupied, which corresponds to a local 0.5 coverage. A rate for these processes was estimated from data given in the two papers of Lossev and Kueppers [7,8]. Noting that exposure experiments were performed with fluxes of $5.0 \cdot 10^{12} \text{ cm}^{-2}\text{s}^{-1}$, an approximation for the required rate per adsorption site is readily obtained by multiplying with half of the area of a unit surface cell, as there are two adsorption sites per unit cell. The flux estimation obtained that way and taking into account a given fluence of 10^{14} cm^{-1} at 1L exposure leads to a reasonable time of 1600 s for an exposure of 80L.

3.3. Resulting kMC simulations

To model the exposure experiments [7,8], kMC simulations simultaneously considering surface diffusion, associative desorption, and atomic adsorption as layed out in the Sections 3.2.2, 3.2.3, and 3.2.4 were carried out. With the exception of atomic adsorption processes, all process rates are obtained by assuming an attempt frequency $\nu = 10^{13} \text{ Hz}$ in conjunction with the respective activation energies ΔE according to $\nu \cdot \exp(-\frac{\Delta E}{k_B T})$. Fig. 7 overlays the original data taken from the aforementioned experiments with a plot of the coverage versus the exposure as simulated by our kMC simulations. The green graph depicts the estimated error in the experimental data of 30%.

4. Discussion

The adopted cluster expansion truncation in Section 3.1 is not perfect, but rather a pragmatic choice. It is the result of only considering a subset of configurations in the original, full training set. The features of the full set could not be captured satisfactorily by any truncation at the same time because of two characteristics. Firstly, there are many different configurations within a very small energy interval directly above the ground state hull. Therefore candidate cluster expansions can easily predict ground state configurations violating the DFT ground state hull. Secondly, several outlier configurations with energies widely above those of the rest in the set are present. For these configurations, hydrogen atoms change their adsorption sites, i.e., they are unstable if allowed to relax freely. Hence, the energy of the final configuration would be wrongly mapped to the initial one by the MAPS code. To avoid this mismatching, only electronic relaxations are considered resulting

in artificial outliers well above the energies of the other fully relaxed configurations. Besides this special treatment, the final configurations are also added to the training set if not yet included. This implies that the cluster expansion assigns high energies to the unstable initial configurations. As a compromise we attempted to keep the outliers in the set using an additional user-supplied weighting scheme patched into MAPS. However, this leads to very small weights for the outliers, if the ground state hull integrity is to be preserved. Therefore we used another approach. We found the reason of the instability is the repulsion of first nearest neighbor hydrogen atoms which relax to adsorption sites further apart. Ultimately, such configurations were left out altogether and their instability were reflected by the introduction of “instantaneous” surface diffusion processes alone. As a result, the CE truncation based on the remaining stable configurations reproduces the DFT GS hull.

For certain 0.5 coverage occupations, significant first layer Be reconstruction softens, and even completely takes away, the notion of a parent lattice, cf. Fig. 5e. Although our cluster expansion and barrier estimations include all the effects of ionic relaxations, our kMC simulations are constrained to the parent lattice. If hydrogen and beryllium atoms relax in a way that is incompatible with the parent lattice, we have to implement these effects in some effective manner. Such a representation is obtained by adopting suitable heuristics when implementing corresponding physical processes. For example, the barrier estimation corresponding to desorption from the reconstructed slab is used in our kMC simulations when sufficient amounts of hydrogen are located in the immediate vicinity of the desorbing atoms.

The high energy barriers associated with dissociative adsorption as found in Section 3.2.1 are in line with experiments reporting the absence of measurable amounts of adsorbed H after exposure to D_2 fluxes at low temperatures [8]. The authors actually give an even higher estimation of $> 1.0 \text{ eV}$, although without an actual measurement. In fact, assuming Maxwell–Boltzmann velocity distributions and completely neglecting vibrational and rotational degrees of freedom, only a small proportion of D_2 carries sufficient kinetic energy to overcome barriers of $\approx 0.85 \text{ eV}$ for a wide range of temperatures, e.g. even at 1600K only $\approx 0.6\%$ of impinging D_2 would contribute.

Simulating macroscopic time scales, e.g. many hundred seconds of exposure time, requires special treatment of very fast microscopic processes, which in our case are surface diffusion processes (see Table 1). These processes were slowed down by means of artificially enlarged diffusion barriers. We increased all surface diffusion barriers by offsets ranging from 0.405 eV to 0.495 eV. This results in a deliberate slowdown corresponding to ≈ 17.38 to ≈ 0.09 surface diffusion events per atomic adsorption event on the clean surface. Note that this assessment concerns the lower bound of surface diffusion on a clean surface only, i.e. a diffusion hop away from an fcc to an adjacent hcp site. This is a typical situation at the very beginning of a simulation run when coverages are still small. With the simulation advancing in time, atomic adsorption increases the coverage, and typical diffusion hops become more frequent due to interactions with surrounding hydrogen being captured by the linear interpolation of diffusion barriers. For the lowest barrier offset (0.405 eV), the system’s time evolution was dominated by surface diffusion events ($\geq 95\%$) from 15L on. Even for the highest barrier offset (0.495 eV), the proportion of surface diffusion events saturated around 80% from about 50L on. Thus, surface diffusion still dominates the time evolution of the system once at least moderate coverages have been reached. In general, slowing the fastest processes down even severely does not necessarily come with adverse effects on the simulation results [31] which are still reliable if sufficiently many fastest events occur between rarer events. In that sense, fast processes are still “fast enough” if

they are able to equilibrate the system between the rare events. In our case, surface diffusion conveys the repulsion amongst adsorbed H and thus establishes a uniform distribution of H on the surface. This however is irrelevant at low coverages because atomic adsorption itself tends to result in uniform H distribution due to taking place with equal probability at every adsorption site. From moderate coverages on, the main effect of surface diffusion is to break up second nearest neighbor interactions as hinted in Fig. 4a and Fig. 4c. This break up still does take place as can be deduced from the increasing proportion of diffusion events in the total system evolution mentioned before. First nearest neighbor H is of no concern as it is guaranteed to be minimal by the adopted “instantaneous” processes. In fact, the slight deviation in the coverage growth and saturation level when considering the biggest slowdown offset can be understood along this line of thought. As mentioned in Section 3.2.4, adsorption sites framed by triangles of second nearest neighbor H contribute additional effective desorption processes. Break up of such second nearest neighbor H needs to be done by regular surface diffusion events. As a result, there are more frequent effective desorption events when surface diffusion becomes too slow and a more shallow increase in coverage is observed. Despite a small deviation in coverage of about 0.01 to 0.02 in the high coverage region, a comparison of the simulation data in Fig. 7 shows little impact of these qualitatively different situations at the beginning of the runs when the surface was still very clean.

The appropriate coverage to compare our results with is given by the experimental, total “coverage”, depicted by the solid black line in the background of Fig. 7. This curve includes surface and, as deduced by the authors, subsurface deuterium. As our simulations do not consider subsurface sites explicitly, the resulting fraction of H must still be considered as residing on the surface in our simulations. Although the simulated coverage at 80L is close to the upper bound of the estimated experimental error of $\approx 30\%$, the overlay shows considerable discrepancies between both results. Most notably, a too small initial slope, followed by a coverage uptake too steep compared to the experimental data and a saturation-like coverage of approximately 0.38 are apparent. The smaller initial slope might be due to an underestimated flux of H to the surface. Another contribution decreasing the initial slope could be an overestimation of effective desorption events by atomic H impinging at already occupied surface sites as a result of neglecting subsurface site occupations. We particularly do not attribute any of these effects to the surface diffusion slowdown, however. While a faster surface diffusion would result in more such events between consecutive atomic adsorption events, the generated time steps should shrink appropriately due to their reciprocal dependence on the total rate. Also, no pronounced dependence on the surface diffusion slowdown is observed comparing the different simulations in Fig. 7. The steeper coverage uptake becomes apparent around exposures of 8L. At this coverage, the onset of measurable absorption in addition to adsorption of H was observed in the experiment. The onset of absorption might be explained by the considerable acceleration of H by interacting with the surface, which is attributed to a polarization effect due to the surface layer relaxations. Molecular dynamics calculations showed accelerated H was able to penetrate the surface, leading to non-negligible subsurface site occupations. Subsequently impinging H might then increasingly hinder the diffusion of adsorbed H towards the surface. This however would also imply an overestimation of effective desorption due to H impinging on occupied surface sites. It is noteworthy that none of the associative desorption processes as shown in Section 3.2.3 play any role in the simulated behavior, as their high energy barriers prevent them from actually being executed in the performed runs. The steeper uptake in coverage is therefore attributed to missed desorption channels, arguably incorporating subsurface site occupations. Fur-

ther processes involving “active sites” on the surface might be of considerable importance, too. Such sites could be the result of self-adsorbed individual Be or other impurities, more complex surface obstacles like steps, individual vacant surface beryllium sites and even trenches, etc. While in principle these influences could be faithfully incorporated into our simulation approach on an equal footing, this requires considerable additional work including a new multicomponent cluster expansion.

Another major source of deviation might be ad- and desorption on a Be O layer which is always experimentally observed on beryllium surface. This, just like the surface obstacles, requires similar comprehensive additional efforts to be accounted for within our simulation approach.

5. Conclusions and outlook

In conclusion, our calculations show that our model captures general trends of the experimentally observed surface deuterium coverage. We tentatively attribute the deviations to the negligence of subsurface site occupations as well as missed desorption processes. We believe that our model in general can be extended accordingly to overcome those shortfalls and account for processes as contemplated in the discussions above. Further searches for desorption processes incorporating surface imperfections and subsurface H might require the implementation of saddle point search algorithms more reliable than the contemporary dimer method.

Acknowledgements

This work has been carried out within the framework of the EUROfusion Consortium and has received funding from the Euratom research and training programme 2014–2018. The views and opinions expressed herein do not necessarily reflect those of the European Commission.

References

- [1] K. Ioki, V. Barabash, A. Cardella, F. Elio, Y. Gohar, G. Janeschitz, G. Johnson, G. Kalinin, D. Lousteau, M. Onozuka, R. Parker, G. Sannazzaro, R. Tivey, *J. Nucl. Mater.* 258–263, Part 1 (1998) 74–84.
- [2] Y. Poitevin, L. Boccaccini, M. Zmitko, I. Ricapito, J.-F. Salavy, E. Diegele, F. Gabriel, E. Magnani, H. Neuberger, R. Lsser, L. Guerrini, *Fusion Eng. Des.* 85 (10–12) (2010) 2340–2347.
- [3] P. Vladimirov, D. Bachurin, V. Borodin, V. Chakin, M. Ganchenkova, A. Fedorov, M. Klimenkov, I. Kupriyanov, A. Moeslang, M. Nakamichi, T. Shibayama, S.V. Til, M. Zmitko, *Fusion Sci. Technol.* 66 (1) (2014) 28–37.
- [4] M. Klimenkov, V. Chakin, A. Moeslang, R. Rolli, *J. Nuclear Mater.* 443 (1–3) (2013) 409–416.
- [5] V. Chakin, Z.Y. Ostrovsky, *J. Nucl. Mater.* 307–311, Part 1 (2002) 657–663.
- [6] V. Chakin, A. Posevin, I. Kupriyanov, *J. Nucl. Mater.* 367–370, Part B (2007) 1377–1381.
- [7] V. Lossev, J. Kppers, *J. Nucl. Mater.* 196–198 (1992) 953–957.
- [8] V. Lossev, J. Kppers, *Surf. Sci.* 284 (1–2) (1993) 175–185.
- [9] K. Pohl, E.W. Plummer, *Phys. Rev. B* 59 (1999) R5324–R5327.
- [10] S. Vagin, P. Chakrov, B. Utkelbayev, L. Jacobson, R. Field, H. Kung, *J. Nucl. Mater.* 258–263, Part 1 (1998) 719–723.
- [11] W.V. Renterghem, A. Leenaers, S.V. denBerghe, *J. Nucl. Mater.* 374 (1–2) (2008) 54–60.
- [12] M. Oberkofler, M. Reinelt, S. Lindig, C. Linsmeier, *Nucl. Instrum. Methods Phys. Res. Sect. B* 267 (4) (2009) 718–722.
- [13] M. Reinelt, A. Allouche, M. Oberkofler, C. Linsmeier, *New J. Phys.* 11 (4) (2009) 043023.
- [14] M. Oberkofler, C. Linsmeier, *Journal of Nuclear Materials* 415 (1, Supplement) (2011) S724–S727.
- [15] M. Reinelt, C. Linsmeier, *Physica Scripta* 2007 (T128) (2007) 111.
- [16] M. Lazzari, S. de Gironcoli, *Surf. Sci.* 402–404 (1998) 715–718.
- [17] P. Hofmann, K. Pohl, R. Stumpf, E.W. Plummer, *Phys. Rev. B* 53 (1996) 13715–13719.
- [18] R. Stumpf, P.J. Feibelman, *Phys. Rev. B* 51 (1995) 13748–13759.
- [19] D. Bachurin, P. Vladimirov, *Surf. Sci.* 641 (2015) 198–203.
- [20] Y. Li, Y. Yang, B. Sun, Y. Wei, P. Zhang, *Phys. Lett. A* 375 (24) (2011) 2430–2436.
- [21] A. Allouche, *Phys. Rev. B* 78 (2008) 085429.
- [22] P.J. Feibelman, *Phys. Rev. B* 48 (1993) 11270–11276.
- [23] G. Kresse, J. Hafner, *Phys. Rev. B* 47 (1993) 558–561.
- [24] G. Kresse, J. Furthmüller, *Phys. Rev. B* 54 (1996) 11169–11186.

- [25] P.E. Blöchl, Phys. Rev. B 50 (1994) 17953–17979.
- [26] G. Kresse, D. Joubert, Phys. Rev. B 59 (1999) 1758–1775.
- [27] J.P. Perdew, Y. Wang, Phys. Rev. B 45 (1992) 13244–13249.
- [28] M. Methfessel, A.T. Paxton, Phys. Rev. B 40 (1989) 3616–3621.
- [29] J. Sanchez, F. Ducastelle, D. Gratias, Physica A 128 (1) (1984) 334–350.
- [30] G. Henkelman, H. Jansson, J. Chem. Phys. 111 (15) (1999) 7010–7022.
- [31] A. Jansen, Lecture OPTnotes in Physics, 2012.
- [32] K. Momma, F. Izumi, VESTA3 for three-dimensional visualization of crystal, volumetric and morphology data, J. Appl. Crystallogr. 44 (6) (2011) 1272–1276.
- [33] Jmol: an open-source java viewer for chemical structures in 3d, URL: <http://www.jmol.org/>